STRUCTURAL BIOLOGY COMMUNICATIONS

ISSN 2053-230X

Conformational heterogeneity in apo and drug-bound structures of *Toxoplasma gondii* prolyl-tRNA synthetase

Siddhartha Mishra,[a] Nipun Malhotra,[a] Shreya Kumari,[a] Mizuki Sato,[b] Haruhisa Kikuchi,[b] Manickam Yogavel[a] and Amit Sharma[a]*

[a]Structural Parasitology, International Centre for Genetic Engineering and Biotechnology, New Delhi, Aruna Asaf Ali Marg, New Delhi, Delhi 110067, India, and [b]Graduate School of Pharmaceutical Sciences, Tohoku University, 6-3 Aza-Aoba, Aramaki, Aoba-ku, Sendai 980-8578, Japan. *Correspondence e-mail: amit.icgeb@gmail.com

Received 5 August 2019
Accepted 1 November 2019

Edited by M. W. Bowler, European Molecular Biology Laboratory, France

Keywords: toxoplasmosis; prolyl-tRNA synthetase; enzyme–inhibitor complexes; comparative crystallography; drug design; r.m.s.d. per residue profile; apo–holo transistions.

PDB references: *T. gondii* prolyl-tRNA synthetase, apo form, 6aa0; complex with febrifugine and ATP analog, 6a88

Supporting information: this article has supporting information at journals.iucr.org/f

Prolyl-tRNA synthetase (PRS) is a member of the aminoacyl-tRNA synthetase family that drives protein translation in cells. The apicomplexan PRSs are validated targets of febrifugine (FF) and its halogenated derivative halofuginone (HF). PRSs are of great interest for drug development against *Plasmodium falciparum* and *Toxoplasma gondii*. In this study, structures of apo and FF-bound *T. gondii* (*Tg*PRS) are revealed and the dynamic nature of the conformational changes that occur upon FF binding is unraveled. In addition, this study highlights significant conformational plasticity within two different crystal structures of apo PRSs but not within drug-bound PRSs. The apo PRSs exist in multi-conformational states and manifest pseudo-dimeric structures. In contrast, when FF is bound the PRS dimer adopts a highly symmetrical architecture. It is shown that *Tg*PRS does not display extant fold switching, in contrast to *P. falciparum* PRS, despite having over 65% sequence identity. Finally, structure-comparison analyses suggest the utility of r.m.s.d. per residue (r.m.s.d.$^{/res}$) as a robust tool to detect structural alterations even when the r.m.s.d. is low. Apo *Tg*PRS reveals FF/HF-induced rigidity and this work has implications for drug-design studies that rely on the apo structures of target proteins.

1. Introduction

The Chinese herb *Dichroa febrifuga* has been used to treat malaria for many centuries (Koepfli *et al.*, 1947). The active compound in the herb was discovered to be a quinazolinone-type alkaloid later named febrifugine (FF; Coatney *et al.*, 1950). As FF is highly toxic, a less toxic derivative of FF called halofuginone (HF) was developed (Hewitt *et al.*, 1952). The inhibitory target of FF and HF was later determined to be prolyl-tRNA synthetase (PRS), a member of the aminoacyl-tRNA synthetase (aaRS) family (Kikuchi *et al.*, 2006; Keller *et al.*, 2012; Son *et al.*, 2013); Zhou *et al.*, 2013; Jain *et al.*, 2014, 2015; Jain, Yogavel *et al.*, 2017). Parasite aaRSs, *i.e.* aaRSs that are encoded in the genome of parasites for protein translation, are being studied as valuable targets in multiple pathogenic organisms that cause malaria, leishmaniasis, toxoplasmosis, cryptosporidiosis and coccidiosis (Bhatt *et al.*, 2009; Jackson *et al.*, 2011; Khan *et al.*, 2011, 2013, 2014; Hoepfner *et al.*, 2012; Gowri *et al.*, 2012; Koh *et al.*, 2012, 2013; Hoen *et al.*, 2013; Pasaje *et al.*, 2016; Jain *et al.*, 2014, 2015; Pham *et al.*, 2014; Hussain *et al.*, 2015; Herman *et al.*, 2015; Kato *et al.*, 2016; Sonoiki *et al.*, 2016; Sharma *et al.*, 2016; Palencia *et al.*, 2016; Jain, Yogavel *et al.*, 2017; Jain, Sharma *et al.*, 2017; Das *et al.*, 2018; Manickam *et al.*, 2018; Nachiappan *et al.*, 2018). *Toxoplasma gondii* is an obligate intracellular parasite that is the

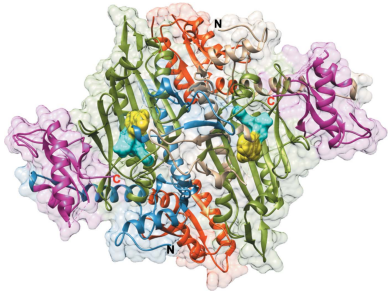

Table 1
Summary of data-collection and refinement statistics.

Values in parentheses are for the highest resolution shell.

	Apo *Tg*PRS (PDB entry 6aa0)	*Tg*PRS–FF–AMPPNP (PDB entry 6a88)
Data collection		
Beamline	PROXIMA 2A, SOLEIL	PROXIMA 1, SOLEIL
Wavelength (Å)	0.980066	0.97857
Detector type	EIGER X 9M	PILATUS 6M
Crystal-to-detector distance (mm)	394.0	393.4
Oscillation (°)	0.1	0.1
Exposure (s)	0.1	0.1
No. of images	3600	3600
Data-processing software	*xia2*/*DIALS*	*xia2*/*DIALS*
a, *b*, *c* (Å)	113.0, 113.0, 119.8	76.9, 90.8, 93.0
α, β, γ (°)	90, 90, 120	89.9, 80.2, 75.5
Space group	$P3_1$	$P1$
Resolution (Å)	97.91–3.20 (3.28–3.20)	42.83–2.60 (2.67–2.60)
R_{merge}	0.163 (0.847)	0.108 (0.602)
R_{meas}	0.172 (0.89)	0.128 (0.73)
No. of unique reflections	47193 (3515)	73015 (5337)
Completeness (%)	100 (100)	98.8 (98.1)
Multiplicity	10.8 (10.7)	3.4 (3.2)
$\langle I/\sigma(I)\rangle$	10.3 (2.7)	7.6 (2.5)
$CC_{1/2}$	0.996 (0.844)	0.987 (0.675)
Refinement		
Resolution	69.9–3.0 (3.09–3.03)	39.9–2.38 (2.40–2.38)
No. of reflections		
Work set	52197 (2611)	90423 (2739)
Test set	2782 (140)	4608 (128)
R_{work}/R_{free}	0.229/0.268	0.184/0.227
Model quality		
R.m.s.d., bond lengths (Å)	0.005	0.007
R.m.s.d., bond angles (°)	0.649	0.719
Ramachandran statistics		
Favoured (%)	92.77	96.96
Allowed (%)	5.94	2.78

cause of toxoplasmosis. We previously solved the crystal structure of HF-bound *T. gondii* PRS (*Tg*PRS) at ∼2.2 Å resolution and showed that HF inhibited *T. gondii* with an EC_{50} of 0.94 n*M*, while FF did so with an EC_{50} of ∼4 n*M* (Jain *et al.*, 2014, 2015; Jain, Yogavel *et al.*, 2017). HF acts by mimicking the PRS substrates L-proline and the adenine moiety of the CCA arm of tRNA; it thus occupies two substrate-binding pockets (Kikuchi *et al.*, 2006; Keller *et al.*, 2012; Son *et al.*, 2013; Zhou *et al.*, 2013; Jain *et al.*, 2014, 2015; Jain, Yogavel *et al.*, 2017).

*Tg*PRS is a homodimeric enzyme whose final product is a tRNA molecule charged with its cognate amino acid proline (Jain *et al.*, 2015; Jain, Yogavel *et al.*, 2017; Jain, Sharma *et al.*, 2017). Here, we have solved two crystal structures of *Tg*PRS in the apo state and in the FF-bound state. We provide an analysis of the conformational heterogeneity observed within two distinct apo *Tg*PRS structures. We also reveal substantial conformational changes that occur upon FF binding in *Tg*PRS. Conformationally heterogeneous landscapes in aaRS proteins have been studied previously in the context of the KMSKS loop of tyrosine-tRNA synthetases (Datt & Sharma, 2014). Relatedly, between 0.5% and 4% of proteins are known to exhibit extant fold-switching (Porter & Looger, 2018). Extant fold-switching occurs as a response to cellular stimuli that include, but are not limited to, the binding of cofactors, ligands or drugs, their concentrations, pH shifts or functional necessity (Porter & Looger, 2018). In particular, class D fold-switching is defined as when the oligomeric states of the apo and the holo forms are identical but the corresponding constituent secondary-structure elements differ. The apicomplexan PRS from *Plasmodium falciparum* has been shown to belong to the class D fold-switchers (Jain *et al.*, 2014, 2015; Jain, Yogavel *et al.*, 2017; Porter & Looger, 2018). Our current work provides new insights into the extant fold-switching phenomenon, as we observe no evidence for this in *Tg*PRS (Porter & Looger, 2018). This is surprising as *T. gondii* and *P. falciparum* are highly related apicomplexan parasites and the two PRSs share ∼64.6% sequence identity.

We observed high symmetry within monomeric PRS protomers when bound to FF, but not in monomeric apo PRSs. Our data provide evidence for ligand-induced fit as well as for drug-induced rigidity in *Tg*PRS when bound to FF. Structural comparisons of the apo and FF-bound structures suggest that induced fit and conformational selection, which are two widely accepted mechanisms for protein–ligand interactions, now regarded as within the extended conformational selection model, are manifest in *Tg*PRS. Finally, structure-comparison analyses based on the r.m.s.d. per residue (r.m.s.d.$^{/res}$) show that this tool is more robust for revealing structural alterations than the use of the r.m.s.d. alone.

2. Methods

2.1. Protein purification, crystallization and structure determination

Purification and crystallization of *Tg*PRS was performed in accordance with previously published methods (Jain *et al.*, 2014, 2015; Jain, Yogavel *et al.*, 2017). Diffraction-quality crystals of apo *Tg*PRS were obtained in Morpheus (Molecular Dimensions) condition D3, while crystals of the *Tg*PRS–FF–AMPPNP complex grew in Morpheus II (Molecular Dimensions) condition E9. Diffraction data were collected on the PROXIMA 1 and 2A beamlines at Synchrotron SOLEIL, France. A total of 3600 frames were collected in 0.1° oscillation steps with 0.1 s exposure per frame. The data were processed and scaled using *DIALS* (Winter *et al.*, 2018) and the relevant statistics are summarized in Table 1. The structures were solved by molecular replacement, with apo *Tg*PRS (PDB entry 5xif; Jain, Yogavel *et al.*, 2017) as a search model for the apo structure. The structure of *Tg*PRS–HF–AMPPNP (PDB entry 5xiq; Jain, Yogavel *et al.*, 2017) was used as a search model for *Tg*PRS–FF–AMPPNP. All structures were solved with *Phenix* (Adams *et al.*, 2010). X-ray refinement restraint parameters were generated for the ligand febrifugine using the *grade* web server (http://grade.globalphasing.org). These were subsequently refined using *phenix.refine*. NCS was not used during refinement, but TLS was. The atomic structures were subjected to refinement cycles using simulated annealing (Cartesian) for three cycles. This was used to remove model bias. After each step, the models were manually

Table 2
Unit-cell parameters and space group along with R_{work}/R_{free} values and resolution information for all PDB entries compared in this study.

	*Tg*PRS, Apo1 (PDB entry 5xif)	*Tg*PRS, Apo2 (PDB entry 6aa0)	*Tg*PRS–HF–AMPPNP, Holo1 (PDB entry 5xiq)	*Tg*PRS–FF–AMPPNP, Holo2 (PDB entry 6a88)
a, *b*, *c* (Å)	76.7, 86.4, 97.2	113.0, 113.0, 119.8	76.9, 90.9, 92.9	76.9, 90.8, 93.0
α, β, γ (°)	90, 106.5, 90	90, 90, 120	89.9, 80.9, 75.8	89.9, 80.2, 75.5
Space group	$P12_11$	$P3_1$	$P1$	$P1$
Resolution† (Å)	53.41–2.48 (2.57–2.48)	97.91–3.20 (3.28–3.20)	50.00–2.19 (2.24–2.19)	42.83–2.60 (2.67–2.60)
R_{work}/R_{free}	0.193/0.249	0.229/0.268	0.165/0.207	0.184/0.227

† Values in paretheses are for the highest resolution shell.

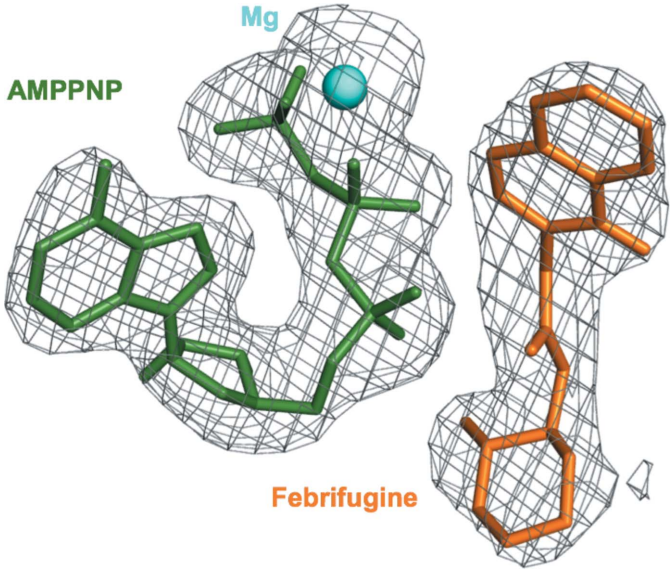

Figure 1
Electron-density fit of FF and AMPPNP. A composite OMIT difference Fourier map ($F_o - F_c$) generated at 2.6 Å and contoured at 1.7σ showing bound FF (coral), AMPPNP (dark green) and the single Mg^{2+} ion (cyan).

adjusted so there was coherence in $2F_o - F_c$ and $F_o - F_c$ electron-density maps. *Coot* (Emsley *et al.*, 2010) was used for all rebuilding. The presence of the ligands was confirmed using OMIT maps (Fig. 1). Model quality was assessed using the *MolProbity* server (Chen *et al.*, 2010). Atomic cooordinates and structure factors have been deposited in the PDB under accession codes 6aa0 and 6a88.

2.2. Structural analyses

In this study, we first analyzed two distinct apo *Tg*PRS structures: Apo1 (PDB entry 5xif) and Apo2 (PDB entry 6aa0). In addition, we studied the *Tg*PRS–HF–AMPPNP co-crystal structure (Holo1; PDB entry 5xiq) and the *Tg*PRS–FF–AMPPNP co-crystal structure (Holo2; PDB entry 6a88). All relevant space-group information is shown in Table 2. We attempted to decrease the bias and be as cautious as possible when analyzing the differences between the two apo structures. Apo1 crystallized in space group $P12_11$, whereas the structure reported here, Apo2, crystallized in space group $P3_1$. The unit-cell dimensions have increased in Apo2 and this is most likely to be due to looser crystal packing in this case. Therefore, the analysis was based on the protomers in the

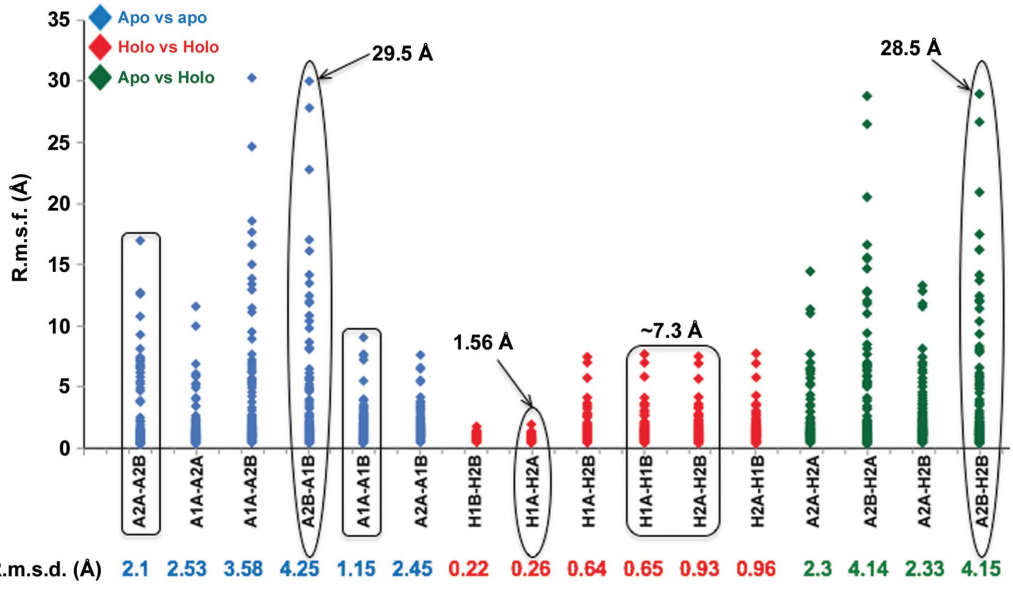

Figure 2
R.m.s.d. versus r.m.s.d.$^{/res}$ analysis of Apo1/2 versus Holo1/2. R.m.s.d.$^{/res}$ variance graphs of the combinations considered in r.m.s.d. analyses are shown. The highest data points representing drastic displacement of the corresponding residues in significant pairs are displayed. The rectangles cover the data sets pointing towards dimeric symmetry within the apo and holo enzymes, while ovals highlight further examined data sets. The corresponding r.m.s.d. values computed from *GESAMT* are noted below the graph. R.m.s.d.$^{/res}$ is labelled r.m.s.f. (fluctuation per residue) to avoid confusion.

biological unit rather than on the entire unit cell. Interestingly, however, the two holo structures both crystallized in space group *P*1 with equivalent unit-cell parameters. This in itself is further proof of the concept of the apo protein being highly flexible and developing drug-induced rigidity upon ligand interaction. A sequence alignment mapping structural differences (electron-density quality and conformational variability) was computed for Apo1 versus Apo2 and for Holo1 versus Holo2 (Supplementary Fig. S1). An alignment of Apo2 versus Holo2 was also computed in the same manner (Supplementary Fig. S2).

Both dimers were compared for r.m.s.d. differences and the aggregate scores displayed a variability of 0.4–0.8 Å between them. Considering ∼1 Å to be a cutoff for biologically significant differences between two structures, it was deemed that what is true for the *AB* dimer also holds for the *CD* dimer. Therefore, only the *AB* chains are discussed as representative models of the structures.

We computed the r.m.s.d. for the protein backbone using the *GESAMT* tool from the *CCP*4 suite (Winn *et al.*, 2011; Krissinel, 2012). This was performed for the eight chains from the four dimers, namely Apo1*A*, Apo1*B*, Apo2*A*, Apo2*B*, Holo1*A*, Holo1*B*, Holo2*A* and Holo2*B*. Furthermore, an r.m.s.d.$^{/res}$ study was performed and a scatter plot was constructed. R.m.s.d.$^{/res}$ values were computed using the structure-alignment tool in *UCSF Chimera* and are indicative of the conformational alterations that a particular residue undergoes.

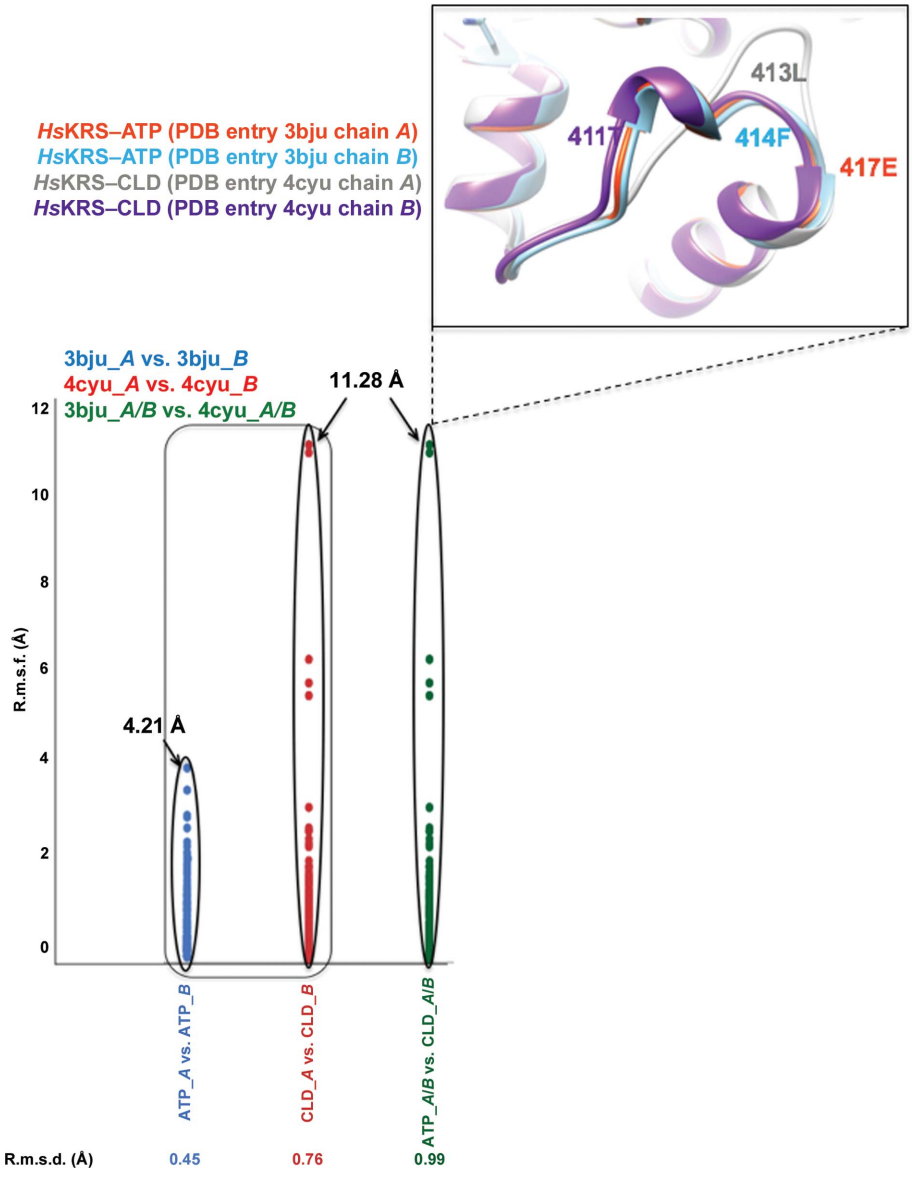

Figure 3
R.m.s.d. versus r.m.s.d.$^{/res}$ analysis of ATP-bound and cladosporin (CLD)-bound forms of *Hs*KRS (PDB entry 3bju versus PDB entry 4ycu). The rectangle covers data sets that point towards dimeric asymmetry within the ATP-bound and CLD-bound enzymes, while the ovals highlight the drastic differences observed between them. The corresponding r.m.s.d. values computed from *GESAMT* are noted below the graph. R.m.s.d.$^{/res}$ is labelled r.m.s.f. (fluctuation per residue) to avoid confusion.

The backbone r.m.s.d. results within each cluster are arranged in a table: apo–apo in blue, holo–holo in red and apo–holo in green (Fig. 2 and Supplementary Fig. S3). The scatter plot for r.m.s.d.$^{/res}$ is presented in the same order as for the r.m.s.d.s (Fig. 2 and Supplementary Fig. S3). Each dot in the graph depicts the r.m.s.d.$^{/res}$ between the corresponding residues in the compared PDB pairs. Thus, the peaks in the histogram indicate higher relative displacement for any given residue pair.

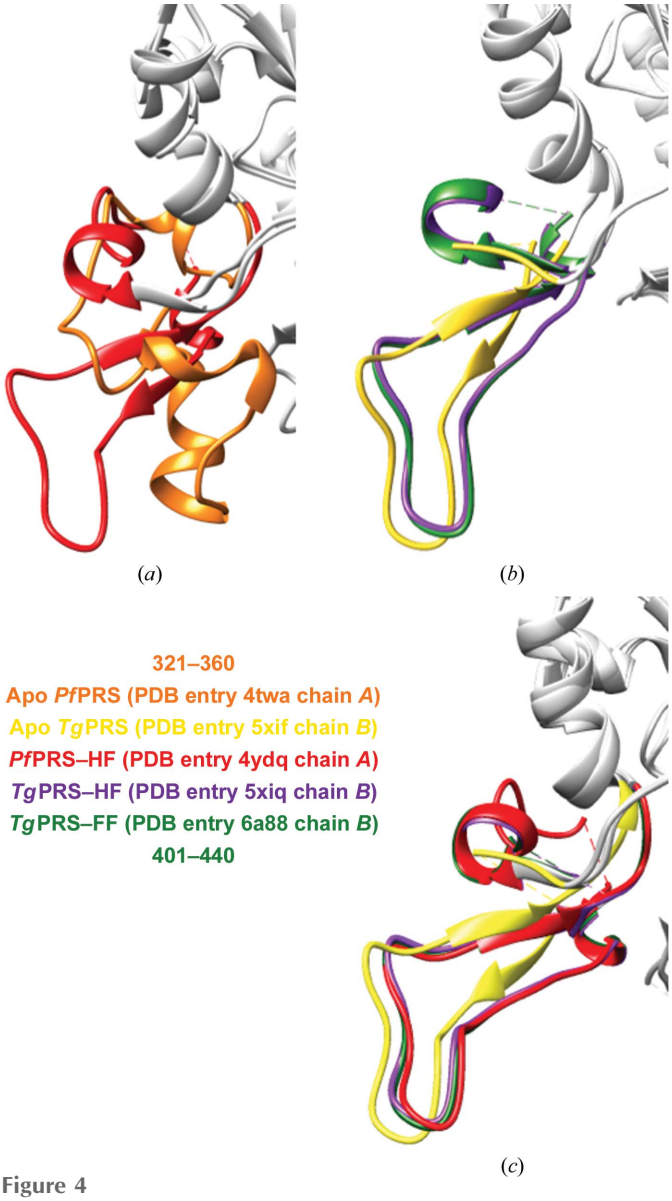

Figure 4
Evidence for fold-switching in *Pf*PRS but not in *Tg*PRS. (*a*) An overlay of monomers of apo *Pf*PRS (PDB entry 4twa; orange) and *Pf*PRS–HF (PDB entry 4ydq; red). The region that displays fold-switching (residues 321–360) is coloured and the rest of the backbone is shown in grey. (*b*) An overlay of monomers of apo *Tg*PRS (PDB entry 5xif; lime yellow), *Tg*PRS–HF (PDB entry 5xiq; purple) and *Tg*PRS–FF (PDB entry 6a88; forest green). The corresponding residues to this region of *Pf*PRS in *Tg*PRS (residues 401–440) are coloured and the rest of the backbone ribbon is shown in grey. (*c*) The corresponding residues of apo *Tg*PRS (PDB entry 5xif; lime yellow), *Pf*PRS–HF (PDB entry 4ydq; red), *Tg*PRS–HF (PDB entry 5xiq; purple) and *Tg*PRS–FF (PDB entry 6a88; forest green) are almost entirely superimposable.

As a control for our r.m.s.d.–r.m.s.d.$^{/res}$ study, we performed the same analyses on a pair of *Homo sapiens* lysyl-tRNA synthetase (*Hs*KRS) structures bound to ATP (PDB entry 3bju) and to cladosporin (PDB entry 4ycu). Our observations here serve as a proof of concept that r.m.s.d.$^{/res}$ is a superior tool to r.m.s.d. when comparing structures that may display small/large conformational changes. R.m.s.d. is the arithmetic mean of the cumulative C^{α} displacement values within the corresponding residues. R.m.s.d.$^{/res}$, on the other hand, is a better way of visualizing the differences between any two structures as the whole breadth of corresponding residue deviations are evident from such an analysis (Figs. 2 and 3).

2.3. Fold-switching and mechanism of drug binding

The apo and HF-bound complexes of *P. falciparum* PRS (*Pf*PRS) have been attested to display fold-switching, which has been observed for related PRSs (Fig. 4*a*; Porter & Looger, 2018). We therefore investigated this for apo and drug-bound structures of *Tg*PRS (Fig. 4*b*). Furthermore, we also analyzed the dimerization loop in the Holo1 and Holo2 dimers in the asymmetric unit. All figures were produced using *UCSF Chimera* (Pettersen *et al.*, 2004)

3. Results and discussion

In this study, the co-crystal structure of *Tg*PRS with FF and adenylyl-imidodiphosphate (AMPPNP) (Holo2) was resolved to 2.6 Å resolution (Table 1; Fig. 5). A new apo *Tg*PRS structure (Apo2) was also resolved to 3.2 Å resolution (Table 1). Direct conformational comparisons were performed with the help of the previously published apo *Tg*PRS (Apo1; PDB entry 5xif) and *Tg*PRS–HF (Holo1; PDB entry 5xiq) structures at 2.4 and 2.1 Å resolution, respectively (Jain, Yogavel *et al.*, 2017). These four structures therefore provided

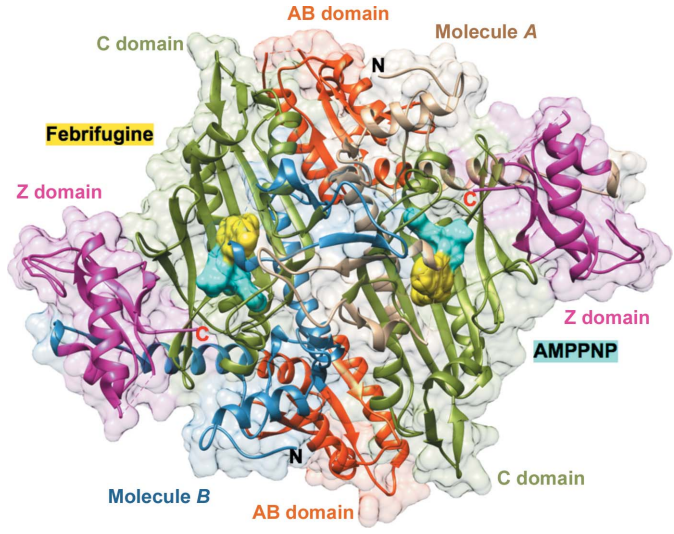

Figure 5
*Tg*PRS–FF–AMPPNP in the asymmetric unit of the crystal. A dimer with bound FF (yellow) and AMPPNP (labeled ANP; cyan). The catalytic (C) domains (residues 434–602), anticodon-binding (AB) domains (residues 621–717) and C-terminal zinc-binding-like (Z) domains (residues 744–832) are labeled, as are the protein termini.

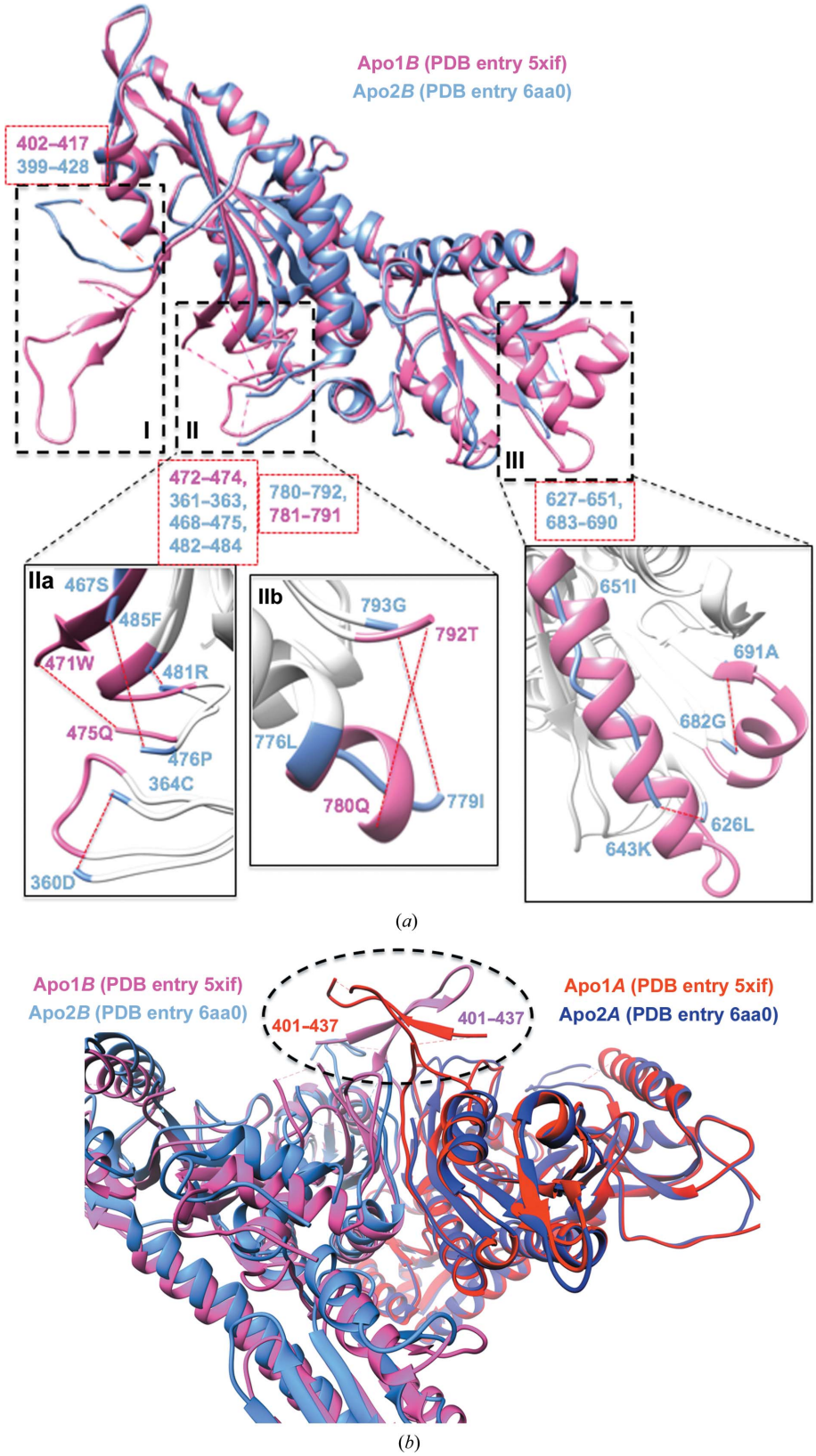

Figure 6
Structural overlays of apo and holo *Tg*PRS. (*a*) Superposition of the Apo1*B* (PDB entry 5xif; hot pink) and Apo2*B* (PDB entry 6aa0; cornflower blue) *Tg*PRS structures with structural differences highlighted. Close-up views of the key differences are shown in I, II and III. The missing residues in Apo1*B* are in regions I (402–417), IIa (472–474) and IIb (781–791). In contrast, Apo2*B* has missing residues in regions I (399–428), IIa (361–363, 468–475 and 482–484), IIb (780–792) and III (627–651 and 683–690). (*b*) Structural comparison of the dimerization hinge among apo *Tg*PRS structures. The dimerization regions (401–437) are ordered in Apo1 but are missing in Apo2. Apo1*A*, red; Apo1*B*, hot pink; Apo2*A*, purple; Apo2*B*, cornflower blue.

us with a platform to assess any conformational changes upon drug (FF/HF) binding in *Tg*PRS.

3.1. Apo1 versus Apo2

Firstly, we undertook a comparison of the Apo1 and Apo2 structures (Fig. 6), in which we observed two key points: the disordered sections in both generally overlap, suggesting higher degrees of freedom in some structural elements within the apoenzyme states and that conformational variability is a function that is more strongly expressed at the boundaries of disordered sections. The r.m.s.d.s of Apo1*A* versus Apo1*B* and of Apo2*A* versus Apo2*B* are of the order of ∼1.15 and ∼2.1 Å, respectively, indicating that the Apo2 dimer is possibly more asymmetric than the Apo1 dimer between the *A* and *B* monomers (Fig. 2, Supplementary Fig. S3). Thus, the apo *Tg*PRSs appear to adopt pseudo-dimeric scaffolds. Our r.m.s.d.$^{/res}$ analysis emphasizes this point as dynamics between the two different apo *Tg*PRS structures and within each apo pseudo-dimer are evident (Fig. 2 and Supplementary Fig. S3). There are numerous structural differences between Apo1*B* and Apo2*B*: highly disordered regions and regions that adopt altered conformations (Fig. 6*a*). The regions revealed to be highly plastic from the alignment include residues 399–437, 469–475, 627–651, 683–690 and 781–791 (Supplementary Fig. S1). Pro429 is strikingly mobile, with an r.m.s.d.$^{/res}$ of ∼29 Å when Apo1*B* and Apo2*B* or Apo2*B* and Holo2*B* are compared. The sections that adopt altered conformations are 429–438 with an average r.m.s.d.$^{/res}$ of 29.5 Å, 643–651 with an average r.m.s.d.$^{/res}$ of 13.7 Å and 776–779 with an average r.m.s.d.$^{/res}$ of 2.4 Å (Figs. 2 and 6*a* and Supplementary Fig. S3). We observed conformational alterations from α-helix to coil-like at residues 643–651 and 776–779.

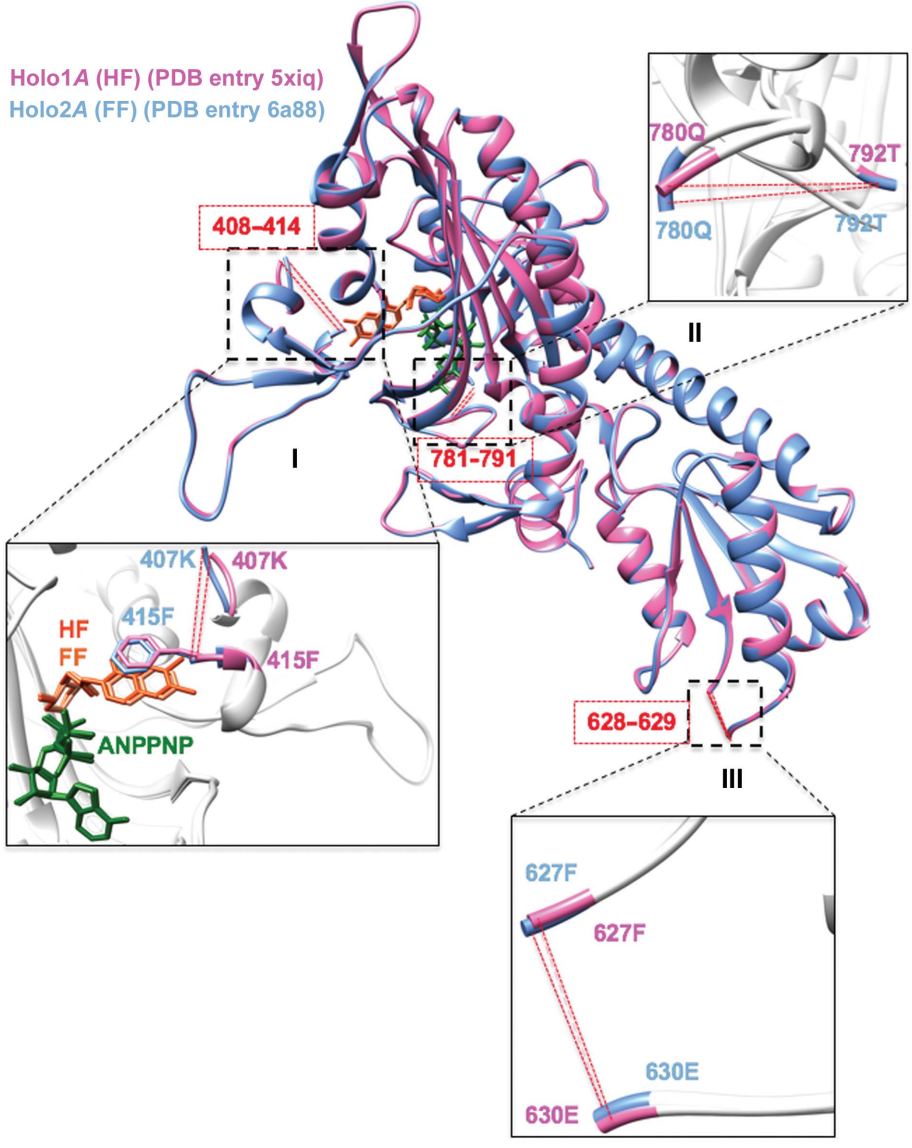

(*c*)

Figure 6 (continued)
Structural overlays of apo and holo *Tg*PRS. (*c*) Structural overlay of the HF-complexed Holo1*A* (PDB entry 5xiq; hot pink) and FF-complexed Holo2*A* (PDB entry 6aa8; cornflower blue) *Tg*PRS structures with structural similarities highlighted. The alignment is divided into three sections: I, II and III. Missing elements (408–414, 628–629 and 781–791) are shown in red.

The solvent content of Apo1 is 53.84% and that of Apo2 is 62.4%. Indeed, it is likely that the conformational differences arise owing to these solvent-content differences, although no discernible influence of crystal packing could be attributed to the conformational differences. Thus, the above analyses revealed significant structural malleability even within apo PRS, which was suggestive of varied global conformations in ligand-free states of *Tg*PRS.

Symmetry within the two protomers of the PRS homodimer has been considered to be a component of a half-site reactivity mechanism (Larson *et al.*, 2012). Half-site reactivity in the context of homodimers can impact k_{cat} (Larson *et al.*, 2012; Fang *et al.*, 2015). This suggests the possibility of structural elements that enable two asymmetric protomers to further dimerize and gain order. Our examination of *Tg*PRS involving inspection of the structures identified loop 401–437 as the dimerization hinge, and there is a corresponding loop in *Pf*PRS (Jain *et al.*, 2014, 2015). This hinge is intrinsically disordered between the Apo1 and Apo2 *Tg*PRS, indicating a higher degree of freedom for this hinge on the basis of electron density. With the exception of Pro429 in Apo1*A*, the integrity of this dimerization interface is intact in both protomers of Apo1 (Fig. 6*b*).

3.2. Holo1 versus Holo2

On the other hand, comparisons of Holo1 and Holo2 confirm that they exhibit high symmetry within the constituent protomers in the dimers. The r.m.s.d.s of Holo1*A* versus Holo1*B* and Holo2*A* versus Holo2*B* are ∼0.65 and ∼0.93 Å, respectively (Fig. 2 and Supplementary Fig. S3). The highest extent of structural alteration (r.m.s.d.$^{/res}$) is only ∼7.3 Å compared with 29.5 Å between the two apo structures (Fig. 2 and Supplementary Fig. S3). Indeed, Holo1*A* and Holo2*A* display insignificant structural differences. Considering that both FF and HF belong to the same chemical class, it is unsurprising that there is a high similarity in structural integrity between FF- and HF-bound PRS structures (Figs. 6*c* and 7). Interestingly, this fidelity is maintained even through different organisms: the active sites of *Tg*PRS–HF, *Tg*PRS–FF and *Pf*PRS–HF are perfectly superimposable (Figs. 4*c* and 6*c* and Supplementary Fig. S1). Binding HF uses two Mg^{2+} ions, whereas binding FF requires only one. Besides this, there is no difference in the interaction between *Tg*PRS or *Pf*PRS and AMPPNP (Figs. 4*c* and 6*c* and Supplementary Fig. S1; Jain, Yogavel *et al.*, 2017).

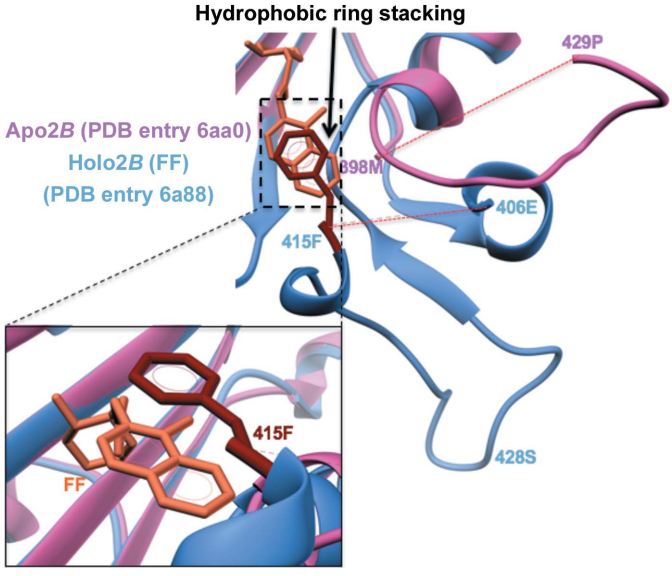

Figure 7
FF-induced active-site loop ordering in *Tg*PRS. The mode of FF binding is similar to that of HF (Jain, Yogavel *et al.*, 2017). Drug-induced loop stabilization of residues 399–428 and π-stacking of Phe415 is clearly visible. In Apo2*B*, this loop is disordered.

3.3. Apo2 versus Holo2

Based on the r.m.s.d. and r.m.s.d.$^{/res}$ plots (Fig. 2 and Supplementary Fig. S3), we next decided to compare the Apo2*B* and Holo2*B* *Tg*PRS (Figs. 7 and 8). The alignment analysis sheds light on the structural transitions that occur between the apo and holo states of *Tg*PRS (Supplementary Fig. S2). Sequence alignment reveals high flexibility of the 399–438, 627–650 and 776–792 regions between the apo and holo states of *Tg*PRS. It also reveals that the binding sites for FF and AMPPNP are disordered in the apo state of *Tg*PRS (Figs. 6*a*, 7 and Supplementary Fig. S2). For ease of understanding, only the holo structure is displayed and the residues that are missing or in a different conformation in Apo2*B* are marked correspondingly (Fig. 8). The conformational changes occur between residues 429 and 438 with an average r.m.s.d.$^{/res}$ of 28.5 Å, between residues 642 and 650 with an average r.m.s.d.$^{/res}$ of 9.9 Å and between residues 776 and 779 with an average r.m.s.d.$^{/res}$ of 3.0 Å (Fig. 2 and Supplementary Fig. S3). The deviation in the position of loop 429–438 is evident in Fig. 8(*b*). Additionally, the conformational alteration of the α-helix cap residues 776–779 is displayed in Fig. 8(*d*). The shift in conformation from α-helix to coil-like for residues 643–650 is indicative of plasticity of the structural elements (Fig. 8*e*).

3.4. Heterogeneity within protomers

Additionally, we analyzed the extent of structural heterogeneity within the two protomers of apo *Tg*PRS. To cover the entire spectrum, we chose the Apo1*B* versus Apo2*B* pair for deeper examination (Fig. 6*a*). This pair showed an r.m.s.d. of 4.25 Å but r.m.s.d.$^{/res}$ values as high as ∼29.5 Å (Fig. 2 and Supplementary Fig. S3). Holo versus holo pairs showed high rigidity and concurrence, with none exceeding an r.m.s.d.$^{/res}$ of ∼7.3 Å, with the lowest alterations observed in Holo1*B* versus Holo2*B*, with r.m.s.d.$^{/res}$ values as low as ∼1.0 Å (Figs. 6*c* and 7 and Supplementary Fig. S3). To remove bias from our own study, we thus chose to further examine Holo1*A* and Holo2*A*, which have an r.m.s.d. of 0.26 Å and a maximum r.m.s.d.$^{/res}$ of 1.56 Å. Apo2*B* versus Holo2*B* shows a backbone r.m.s.d. of 4.15 Å but an r.m.s.d.$^{/res}$ exceeding ∼28 Å (Figs. 2 and 8 and Supplementary Fig. S3).

3.5. Evidence for a lack of extant fold-switching in *Tg*PRS and for an extended-conformational selection model

In the light of a recent publication, we also confirmed fold-switching in apo and HF-bound structures of *Pf*PRS (Porter &

Looger, 2018; Fig. 4*a*). Intriguingly, when the *Tg*PRS apo and drug-bound structures were compared, no evidence of fold-switching was observed (Figs. 4*b* and 8*c*). We noticed no influence of lattice contacts on the ability to fold-switch in the apo/holo protein transitions for *Tg*PRS.

Our work also reiterates the conformational selection model for *Tg*PRS–drug interactions, as one apo *Tg*PRS structure adopts a conformation akin to the FF-bound *Tg*PRS (the same is true for HF-bound *Tg*PRS; Figs. 2 and 4*c*). In addition, there is significant induced fit upon drug

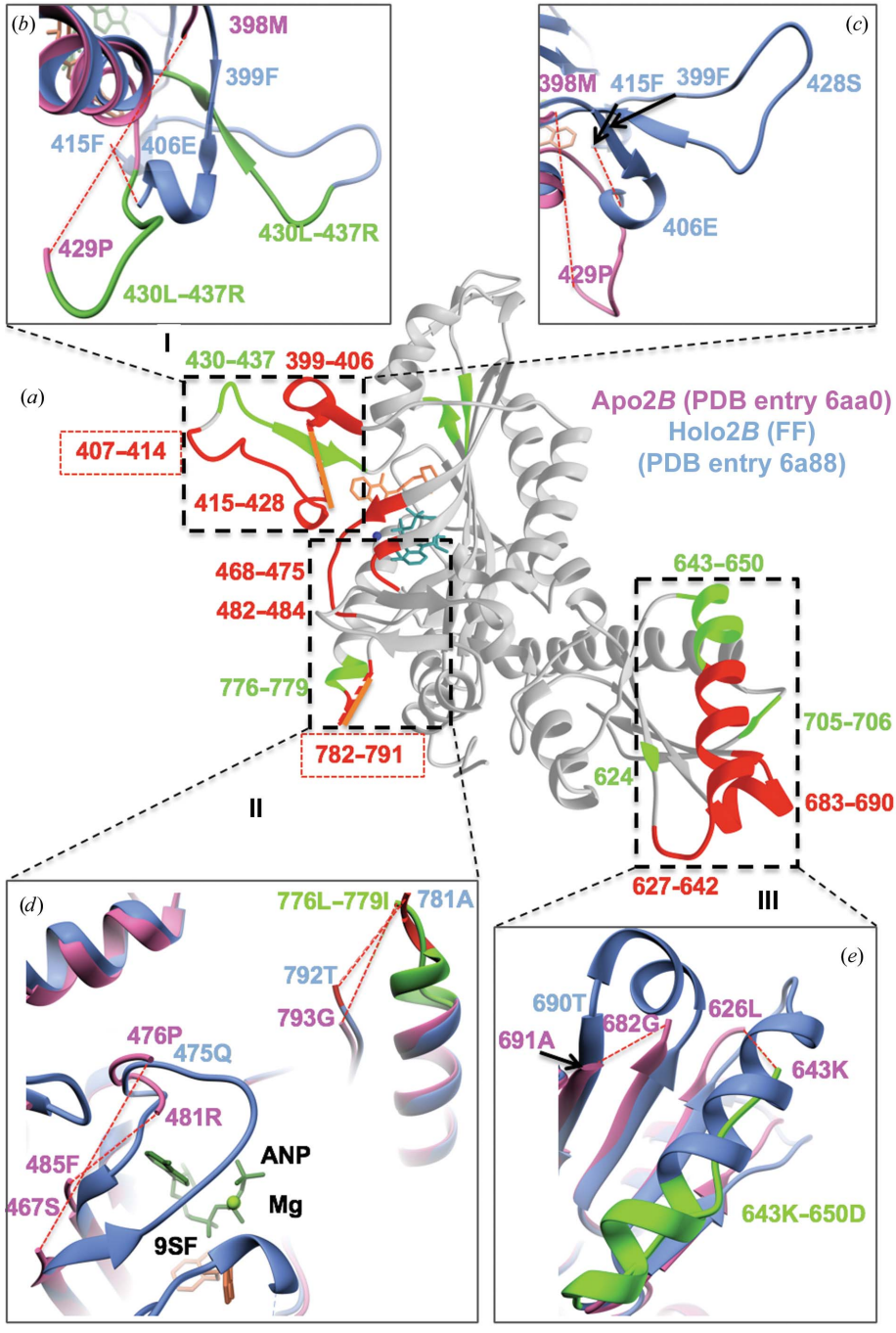

Figure 8
Structural differences between the Apo2*B* and Holo2*B* *Tg*PRS structures. (*a*) FF-complexed Holo2*B* (dark grey) is divided into three sections, I, II and III, based on its structural differences from Apo2*B*. Only the missing residues (red) and those that adopt altered conformations (lime green) in Apo2*B* have been overlaid on Holo2*B*, while the common missing links are represented by a solid orange line. (*b*) Close-up view of the conformationally heterogeneous 430–437 loop in section I. In Apo2*B*, this loop is in a disordered conformation when compared with FF-complexed Holo2*B*. (*c*) Missing residues in Apo2*B* (399–428) and FF-complexed Holo2*B* (407–414) within section I are marked. Arrows represent residues in the background (Phe415 and Phe399). (*d*) Section II depicts the regions 468–475, 482–484 and 780–792 that are missing in Apo2*B*. Residues 782–791 are missing in FF-complexed Holo2*B*. The drastic conformational change in the motif 776–779 is also depicted. (*e*) Close-up view of section III showing the missing regions (627–642 and 683–690) in Apo2*B* along with the conformational differences within the region 643–650.

binding as evident visually and by r.m.s.f. analysis (Figs. 2, 7 and 8).

3.6. Advantages of r.m.s.d.$^{/res}$ over r.m.s.d.

We propose that r.m.s.d.$^{/res}$ analysis is more revealing about global structural changes than r.m.s.d. comparisons (Figs. 2 and 3). While the maximal r.m.s.d.$^{/res}$ values for the apo *Tg*PRS structures are 8.6 and 16.6 Å for Apo1 and Apo2, respectively, those for the holo *Tg*PRSs are ∼7.3 Å (Fig. 2 and Supplementary Fig. S3). This divergence itself is proof of significant structural transitions consequent to the envelopment of FF by *Tg*PRS. The plastic nature of the apo conformations can be contrasted with the rigid framework of the drug-bound enzyme using r.m.s.d.$^{/res}$ data (Fig. 2 and Supplementary Fig. S3). Additionally, we recently extended the r.m.s.d.–r.m.s.d.$^{/res}$ analyses to another set of aaRS structures bound to ATP at 2.3 Å resolution and cladosporin at 2.1 Å resolution (Chhibber-Goel & Sharma, 2019). R.m.s.d.s for ATP-bound *Homo sapiens* lysyl-tRNA synthetase (*Hs*KRS) structures remain below ∼1 Å and the maximum r.m.s.d.$^{/res}$ increases to >11 Å, indicating a large conformational change in limited regions of KRSs (Fig. 3 and Supplementary Fig. S4). The inset in Fig. 3 shows the region that differs conformationally: from Thr411 to Glu417 in *Hs*KRS. Thus, local and global changes in protein structures in various states of ligand engagement can be reliably assessed via a combination of r.m.s.d. and r.m.s.d.$^{/res}$ analyses. The analysis of *Tg*PRS apo/holo structures presented here highlights key issues of structural variance in enzyme states that are vital for consideration in structure-based drug development.

4. Conclusions

The *Tg*PRS enzyme is flexible in ligand-free states, as evident from the two apo structures. Further, upon engagement with FF/HF the enzyme adopts a highly ordered structure in the two protomers that constitute the biological dimer. In contrast to *Pf*PRS, the close evolutionary homologue *Tg*PRS does not display extant fold-switching. This work therefore highlights the conformational heterogeneity inherent within apicomplexan PRSs.

Acknowledgements

The authors thank the beamline staff at PROXIMA 1 and PROXIMA 2A for assistance during data collection at SOLEIL. We thank Dr Rai for inspiration.

Funding information

The following funding is acknowledged: Department of Biotechnology, Ministry of Science and Technology (grant No. PR6303 to Amit Sharma; grant No. PR13636 to Amit Sharma and Manickam Yogavel); Indo–French Centre for the Promotion of Advanced Research (IFCPAR/CEFIPRA; Travel Grant to Manickam Yogavel); Department of Science and Technology, India (award No. SB/S2/JCB-41/2013 to Amit Sharma).

References

Adams, P. D., Afonine, P. V., Bunkóczi, G., Chen, V. B., Davis, I. W., Echols, N., Headd, J. J., Hung, L.-W., Kapral, G. J., Grosse-Kunstleve, R. W., McCoy, A. J., Moriarty, N. W., Oeffner, R., Read, R. J., Richardson, D. C., Richardson, J. S., Terwilliger, T. C. & Zwart, P. H. (2010). *Acta Cryst.* D**66**, 213–221.

Bhatt, T. K., Kapil, C., Khan, S., Jairajpuri, M. A., Sharma, V., Santoni, D., Silvestrini, F., Pizzi, E. & Sharma, A. (2009). *BMC Genomics*, **10**, 644.

Chen, V. B., Arendall, W. B., Headd, J. J., Keedy, D. A., Immormino, R. M., Kapral, G. J., Murray, L. W., Richardson, J. S. & Richardson, D. C. (2010). *Acta Cryst.* D**66**, 12–21.

Chhibber-Goel, J. & Sharma, A. (2019). *Proteins*, **87**, 730–737.

Coatney, G. R., Cooper, W. C., Culwell, W. B., White, W. C. & Imboden, C. A. (1950). *J. Natl Malar. Soc.* **9**, 183–186.

Das, P., Babbar, P., Malhotra, N., Sharma, M., Jachak, G. R., Gonnade, R. G., Shanmugam, D., Harlos, K., Yogavel, M., Sharma, A. & Reddy, D. S. (2018). *J. Med. Chem.* **61**, 5664–5678.

Datt, M. & Sharma, A. (2014). *J. Struct. Funct. Genomics*, **15**, 45–61.

Emsley, P., Lohkamp, B., Scott, W. G. & Cowtan, K. (2010). *Acta Cryst.* D**66**, 486–501.

Fang, P., Han, H., Wang, J., Chen, K., Chen, X. & Guo, M. (2015). *Chem. Biol.* **22**, 734–744.

Gowri, V. S., Ghosh, I., Sharma, A. & Madhubala, R. (2012). *BMC Genomics*, **13**, 621.

Herman, J. D., Pepper, L. R., Cortese, J. F., Estiu, G., Galinsky, K., Zuzarte-Luis, V., Derbyshire, E. R., Ribacke, U., Lukens, A. K., Santos, S. A., Patel, V., Clish, C. B., Sullivan, W. J., Zhou, H., Bopp, S. E., Schimmel, P., Lindquist, S., Clardy, J., Mota, M. M., Keller, T. L., Whitman, M., Wiest, O., Wirth, D. F. & Mazitschek, R. (2015). *Sci. Transl. Med.* **7**, 288ra77.

Hewitt, R. I., Wallace, W. S., Gill, E. R. & Williams, J. H. (1952). *Am. J. Trop. Med. Hyg.* **1**, 768–772.

Hoen, R., Novoa, E. M., López, A., Camacho, N., Cubells, L., Vieira, P., Santos, M., Marin-Garcia, P., Bautista, J. M., Cortés, A., Ribas de Pouplana, L. & Royo, M. (2013). *Chembiochem*, **14**, 499–509.

Hoepfner, D., McNamara, C. W., Lim, C. S., Studer, C., Riedl, R., Aust, T., McCormack, S. L., Plouffe, D. M., Meister, S., Schuierer, S., Plikat, U., Hartmann, N., Staedtler, F., Cotesta, S., Schmitt, E. K., Petersen, F., Supek, F., Glynne, R. J., Tallarico, J. A., Porter, J. A., Fishman, M. C., Bodenreider, C., Diagana, T. T., Movva, N. R. & Winzeler, E. A. (2012). *Cell Host Microbe*, **11**, 654–663.

Hussain, T., Yogavel, M. & Sharma, A. (2015). *Antimicrob. Agents Chemother.* **59**, 1856–1867.

Jackson, K. E., Habib, S., Frugier, M., Hoen, R., Khan, S., Pham, J. S., de Pouplana, L. R., Royo, M., Santos, M. A. S., Sharma, A. & Ralph, S. A. (2011). *Trends Parasitol.* **27**, 467–476.

Jain, V., Kikuchi, H., Oshima, Y., Sharma, A. & Yogavel, M. (2014). *J. Struct. Funct. Genomics*, **15**, 181–190.

Jain, V., Sharma, A., Singh, G., Yogavel, M. & Sharma, A. (2017). *ACS Infect. Dis.* **3**, 281–292.

Jain, V., Yogavel, M., Kikuchi, H., Oshima, Y., Hariguchi, N., Matsumoto, M., Goel, P., Touquet, B., Jumani, R. S., Tacchini-Cottier, F., Harlos, K., Huston, C. D., Hakimi, M. A. & Sharma, A. (2017). *Structure*, **25**, 1495–1505.

Jain, V., Yogavel, M., Oshima, Y., Kikuchi, H., Touquet, B., Hakimi, M. A. & Sharma, A. (2015). *Structure*, **23**, 819–829.

Kato, N., Comer, E., Sakata-Kato, T., Sharma, A., Sharma, M., Maetani, M., Bastien, J., Brancucci, N. M., Bittker, J. A., Corey, V., Clarke, D., Derbyshire, E. R., Dornan, G. L., Duffy, S., Eckley, S., Itoe, M. A., Koolen, K. M. J., Lewis, T. A., Lui, P. S., Lukens, A. K., Lund, E., March, S., Meibalan, E., Meier, B. C., McPhail, J. A., Mitasev, B., Moss, E. L., Sayes, M., Van Gessel, Y., Wawer, M. J., Yoshinaga, T., Zeeman, A. M., Avery, V. M., Bhatia, S. N., Burke, J. E., Catteruccia, F., Clardy, J. C., Clemons, P. A., Dechering, K. J., Duvall, J. R., Foley, M. A., Gusovsky, F., Kocken, C. H. M., Marti, M., Morningstar, M. L., Munoz, B., Neafsey, D. E., Sharma, A.,

Winzeler, E. A., Wirth, D. F., Scherer, C. A. & Schreiber, S. L. (2016). *Nature (London)*, **538**, 344–349.
Keller, T. L., Zocco, D., Sundrud, M. S., Hendrick, M., Edenius, M., Yum, J., Kim, Y. J., Lee, H. K., Cortese, J. F., Wirth, D. F., Dignam, J. D., Rao, A., Yeo, C. Y., Mazitschek, R. & Whitman, M. (2012). *Nature Chem. Biol.* **8**, 311–317.
Khan, S., Garg, A., Camacho, N., Van Rooyen, J., Kumar Pole, A., Belrhali, H., Ribas de Pouplana, L., Sharma, V. & Sharma, A. (2013). *Acta Cryst.* D**69**, 785–795.
Khan, S., Sharma, A., Belrhali, H., Yogavel, M. & Sharma, A. (2014). *J. Struct. Funct. Genomics*, **15**, 63–71.
Khan, S., Sharma, A., Jamwal, A., Sharma, V., Pole, A. K., Thakur, K. K. & Sharma, A. (2011). *Sci. Rep.* **1**, 188.
Kikuchi, H., Yamamoto, K., Horoiwa, S., Hirai, S., Kasahara, R., Hariguchi, N., Matsumoto, M. & Oshima, Y. (2006). *J. Med. Chem.* **49**, 4698–4706.
Koepfli, J. B., Mead, J. F. & Brockman, J. A. (1947). *J. Am. Chem. Soc.* **69**, 1837.
Koh, C. Y., Kim, J. E., Napoli, A. J., Verlinde, C. L. M. J., Fan, E., Buckner, F. S., Van Voorhis, W. C. & Hol, W. G. J. (2013). *Mol. Biochem. Parasitol.* **189**, 26–32.
Koh, C. Y., Kim, J. E., Shibata, S., Ranade, R. M., Yu, M., Liu, J., Gillespie, J. R., Buckner, F. S., Verlinde, C. L. M. J., Fan, E. & Hol, W. G. J. (2012). *Structure*, **20**, 1681–1691.
Krissinel, E. (2012). *J. Mol. Biochem.* **1**, 76–85.
Larson, E. T., Kim, J. E., Napuli, A. J., Verlinde, C. L. M. J., Fan, E., Zucker, F. H., Van Voorhis, W. C., Buckner, F. S., Hol, W. G. J. & Merritt, E. A. (2012). *Acta Cryst.* D**68**, 1194–1200.
Manickam, Y., Chaturvedi, R., Babbar, P., Malhotra, N., Jain, V. & Sharma, A. (2018). *Drug Discov. Today*, **23**, 1233–1240.
Nachiappan, M., Jain, V., Sharma, A., Yogavel, M. & Jeyakanthan, J. (2018). *Int. J. Biol. Macromol.* **120**, 1379–1386.
Palencia, A., Liu, R.-J., Lukarska, M., Gut, J., Bougdour, A., Touquet, B., Wang, E.-D., Li, X., Alley, M. R. K., Freund, Y. R., Rosenthal, P. J., Hakimi, M.-A. & Cusack, S. (2016). *Antimicrob. Agents Chemother.* **60**, 5817–5827.
Pasaje, C. F. A., Cheung, V., Kennedy, K., Lim, E. E., Baell, J. B., Griffin, M. D. W. & Ralph, S. A. (2016). *Sci. Rep.* **6**, 27531.
Pettersen, E. F., Goddard, T. D., Huang, C. C., Couch, G. S., Greenblatt, D. M., Meng, E. C. & Ferrin, T. E. (2004). *J. Comput. Chem.* **25**, 1605–1612.
Pham, J. S., Dawson, K. L., Jackson, K. E., Lim, E. E., Pasaje, C. F. A., Turner, K. E. C. & Ralph, S. A. (2014). *Int. J. Parasitol. Drugs Drug Resist.* **4**, 1–13.
Porter, L. L. & Looger, L. L. (2018). *Proc. Natl. Acad. Sci. USA*, **115**, 5968–5973.
Sharma, A., Sharma, M., Yogavel, M. & Sharma, A. (2016). *PLoS Negl. Trop. Dis.* **10**, e0005084.
Son, J., Lee, E. H., Park, M., Kim, J. H., Kim, J., Kim, S., Jeon, Y. H. & Hwang, K. Y. (2013). *Acta Cryst.* D**69**, 2136–2145.
Sonoiki, E., Palencia, A., Guo, D., Ahyong, V., Dong, C., Li, X., Hernandez, V. S., Zhang, Y.-K., Choi, W., Gut, J., Legac, J., Cooper, R., Alley, M. R. K., Freund, Y. R., DeRisi, J., Cusack, S. & Rosenthal, P. J. (2016). *Antimicrob. Agents Chemother.* **60**, 4886–4895.
Winn, M. D., Ballard, C. C., Cowtan, K. D., Dodson, E. J., Emsley, P., Evans, P. R., Keegan, R. M., Krissinel, E. B., Leslie, A. G. W., McCoy, A., McNicholas, S. J., Murshudov, G. N., Pannu, N. S., Potterton, E. A., Powell, H. R., Read, R. J., Vagin, A. & Wilson, K. S. (2011). *Acta Cryst.* D**67**, 235–242.
Winter, G., Waterman, D. G., Parkhurst, J. M., Brewster, A. S., Gildea, R. J., Gerstel, M., Fuentes-Montero, L., Vollmar, M., Michels-Clark, T., Young, I. D., Sauter, N. K. & Evans, G. (2018). *Acta Cryst.* D**74**, 85–97.
Zhou, H., Sun, L., Yang, X. L. & Schimmel, P. (2013). *Nature (London)*, **494**, 121–124.